

MERLIN observations of relativistic ejections from GRS 1915+105

R.P. Fender^{1*}, S.T. Garrington², D.J. McKay^{2,3}, T.W.B. Muxlow²,
G.G. Pooley⁴, R.E. Spencer², A.M. Stirling², E.B. Waltman⁵

¹ *Astronomical Institute ‘Anton Pannekoek’ and Center for High Energy Astrophysics, University of Amsterdam, Kruislaan 403, 1098 SJ Amsterdam, The Netherlands.*

² *University of Manchester, Nuffield Radio Astronomy Laboratories, Jodrell Bank, Cheshire, SK11 9DL*

³ *Joint Institute for VLBI in Europe, Postbus 2, 7990 AA Dwingeloo, The Netherlands*

⁴ *Mullard Radio Astronomy Observatory, Cavendish Laboratory, Madingley Road, Cambridge CB3 0HE*

⁵ *Remote Sensing Division, Code 7210, Naval Research Laboratory, Washington, D.C. 20375-5351, USA*

23 January 2018

ABSTRACT

We present high resolution MERLIN radio images of multiple relativistic ejections from GRS 1915+105 in 1997 October / November. The observations were made at a time of complex radio behaviour, corresponding to multiple optically-thin outbursts and several days of rapid radio flux oscillations. This activity followed ~ 20 days of a plateau state of inverted-spectrum radio emission and hard, quasi-stable X-ray emission. The radio imaging resolved four major ejection events from the system. As previously reported from earlier VLA observations of the source, we observe apparent superluminal motions resulting from intrinsically relativistic motions of the ejecta. However, our measured proper motions are significantly greater than those observed on larger angular scales with the VLA. Under the assumption of an intrinsically symmetric ejection, we can place an upper limit on the distance to GRS 1915+105 of 11.2 ± 0.8 kpc. Solutions for the velocities unambiguously require a higher intrinsic speed by about $0.1c$ than that derived from the earlier VLA observations, whilst the angle to the line-of-sight is not found to be significantly different. At a distance of 11 kpc, we obtain solutions of $v = 0.98^{+0.02}_{-0.05}c$ and $\theta = 66 \pm 2$ degrees. The jet also appears to be curved on a scale which corresponds to a period of around 7 days.

We observe significant evolution of the linear polarisation of the approaching component, with large rotations in position angle and a general decrease in fractional polarisation. This may be due to increasing randomisation of the magnetic field within the ejected component. We do not at any time detect significant linear polarisation from the core, including periods when the flux density from this region is dominated by radio oscillations. The power input into the formation of the jet is very large, $\geq 10^{38}$ erg s^{-1} at 11 kpc for a pair plasma. If the plasma contains a cold proton for each electron, then the mass outflow rate, $\geq 10^{18}$ g s^{-1} is comparable to inflow rates previously derived from X-ray spectral fits.

Key words:

Accretion, accretion disks – Stars: individual GRS 1915+105 – Stars: variables – ISM: jets and outflows – Radio continuum: stars – X-rays: stars

1 INTRODUCTION

GRS 1915+105 is a distant black-hole-candidate X-ray transient in the Galactic-plane, discovered by the WATCH in-

strument on board the GRANAT mission in 1992 (Castro-Tirado, Brandt & Lund 1992). Owing to large extinction ($A_V \geq 20$ mag), the properties of the optical counterpart are unknown, but observations at radio, near-infrared and X-ray energies have shown GRS 1915+105 to be a highly unusual and energetic system.

* email : rpf@astro.uva.nl

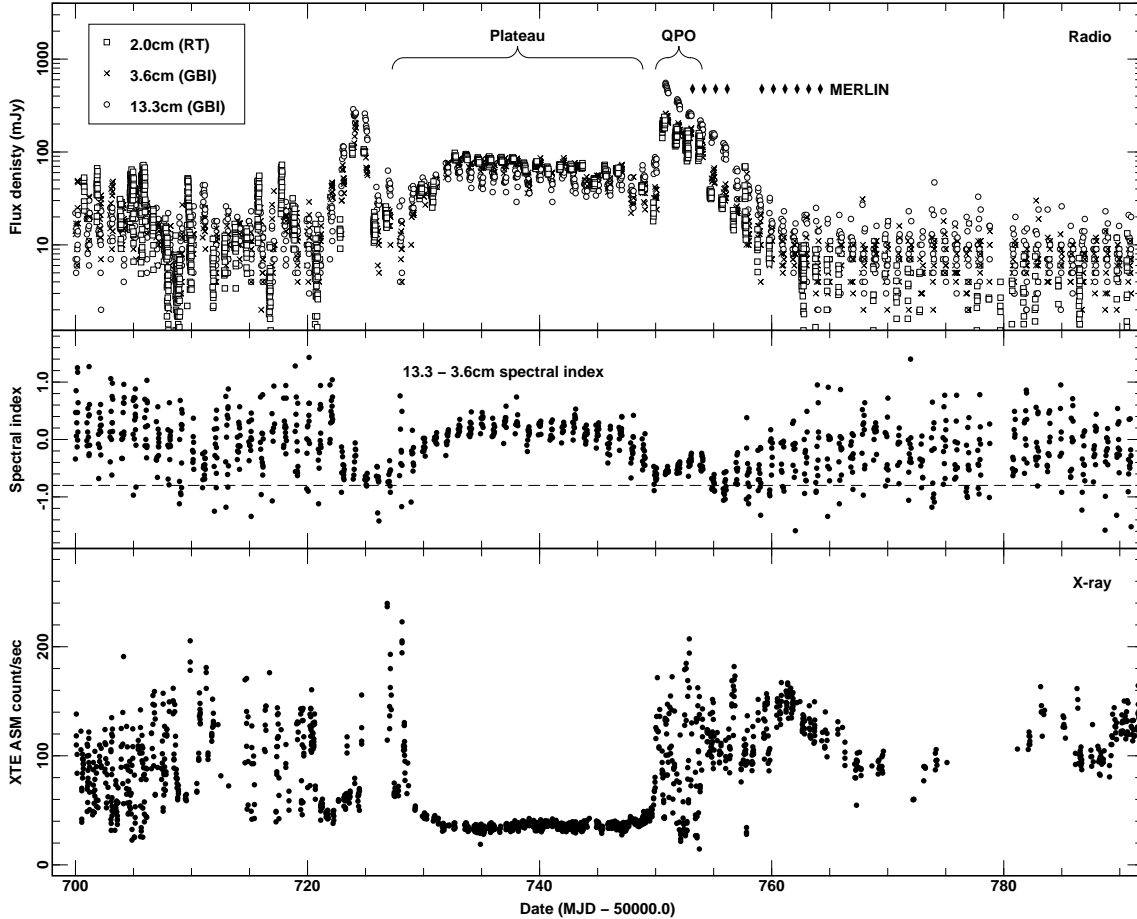


Figure 1. Radio and X-ray flux monitoring spanning the sequence of radio ejections mapped by MERLIN. The upper panel shows the flux densities measured at 2.0 cm with the RT, and at 3.6 cm and 13.3 cm with the GBI. The middle panel shows the radio spectral index from simultaneous measurements at 13.3 and 3.6 cm. The lower panel shows the count rate in the 2–12 keV band by the Rossi X-ray Timing Explorer (RXTE) All-Sky Monitor (ASM). The optically thin state evolves towards a spectral index of -0.8 which is shown by the dashed line in the middle panel.

Shortly after the discovery of the X-ray source, variable radio and infrared counterparts were identified (Mirabel et al. 1994). Subsequent mapping of the radio counterpart following an outburst in 1994 revealed apparent superluminal motions in a two-sided ejection of synchrotron-emitting components from the source (Mirabel & Rodríguez 1994; hereafter MR94). This was the first observation of superluminal motions in our Galaxy, the only previously measured proper motions of ejections from X-ray binaries (SS 433 & Cyg X-3) implying velocities of $\sim 0.3c$. Within a year, a second superluminal source, GRO J1655–40, had been discovered (Tingay et al. 1995; Hjellming & Rupen 1995). A third possible superluminal jet source, XTE J1748–288, has recently been reported (Rupen, Hjellming & Mioduszewski 1998).

The VLA observations of GRS 1915+105 by MR94 revealed proper motions of 17.6 ± 0.4 and 9.0 ± 0.1 mas d^{-1} for two components separating from a core at position angles of 150 and 330° respectively. From HI absorption measurements these authors derived a most likely distance to the source of 12.5 ± 1.5 kpc, giving apparent transverse motions of $1.25c \pm 0.15c$ and $0.65c \pm 0.08c$ respectively. Proper motion and flux density ratios between the (inferred) approaching

and receding components were consistent with simple ballistic bulk motions. Solving for the proper motions at a distance of 12.5 kpc, a true velocity of $0.92c \pm 0.08c$ at an angle of $70 \pm 2^\circ$ to the line-of-sight was derived. Further observations with the VLA following a radio outburst in 1995 revealed relativistic ejection for a second time (Mirabel et al. 1996). However the proper motions and flux density ratios appeared to be somewhat different from those reported in MR94 possibly implying a change in the jet velocity or the angle to the line-of-sight. A summary of multiple VLA observations of major relativistic ejections from GRS 1915+105 is given in Rodríguez & Mirabel (1999; hereafter RM99).

Pooley & Fender (1997; hereafter PF97) report ~ 2 yr of radio monitoring of GRS 1915+105 at 15 GHz with the Ryle Telescope (RT). They describe in detail quasi-periodic radio oscillations with periods typically in the range 20–40 min, a phenomenon not previously seen in any other source, and first reported in Pooley (1995). Fender et al. (1997) report the discovery of infrared counterparts to the radio oscillations, suggesting an approximately flat synchrotron spectrum from cm to μm wavelengths. They proposed that each oscillation corresponds to a small ejection of material

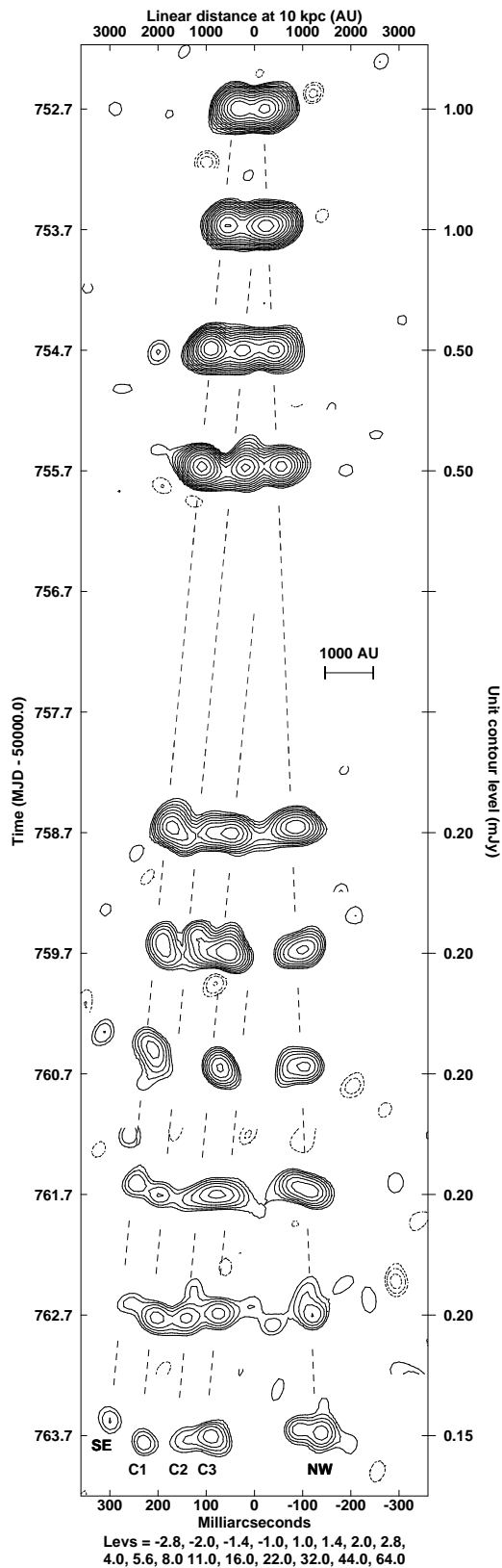


Figure 2. MERLIN maps of total intensity from 10 – 12-hr observations at the epochs illustrated on Fig. 1. The images have been rotated clockwise by 52 degrees to form the montage. Contour levels increase in factors of $\sqrt{2}$ from the unit contour level indicated at the right-hand side of each image. Mapping fidelity is dominated by dynamic range considerations for the first 5 epochs, whilst receiver noise dominates later.

from the GRS 1915+105 system. Around the same time Belloni et al. (1997a,b) proposed that X-ray dips with similar periods correspond to the removal of the inner (≤ 200 km) region of the accretion disc, possibly advected into the black hole. The observation of a correlation between such X-ray dips and the rise of radio oscillations (PF97) seemed to complete a picture of repeated ejection and refill of the inner accretion disc, the ejecta emitting a flat synchrotron spectrum from 2 cm – 2 μ m before they cool due to adiabatic expansion losses. Further X-ray, radio and infrared timing observations (Eikenberry et al. 1998; Mirabel et al. 1998; Fender & Pooley 1998) appear to confirm this model, at least qualitatively.

Long-term comparison of radio and 2–12 keV X-ray light curves in PF97 revealed an unusual period of activity in 1996 July–August, hereafter the ‘plateau’ state, during which time the X-ray emission entered a hard, quasi-stable state, while the radio emission became relatively bright at 15 GHz. Earlier occurrences of this state are reported in Foster et al. (1996) and Harmon et al. (1997). Bandyopadhyay et al. (1998) also discuss bright infrared emission during such periods. It was speculated in PF97 (and earlier, in Harmon et al. 1997) that such plateau states may correspond to major radio ejections from the GRS 1915+105 system. Fig. 1 shows that a significant radio flare occurred around MJD 50725. This was the prelude to a plateau state lasting 20 days in which a bright, apparently optically thick, radio source was formed, coinciding with a quasi-stable, hard X-ray state. At the end of the plateau stage a second, major radio flare occurred which triggered the MERLIN mapping observations, the highest resolution imaging of GRS 1915+105 to date. Each MERLIN map epoch is indicated by a diamond in the upper panel of Fig. 1.

2 OBSERVATIONS

2.1 MERLIN

GRS 1915+105 was observed using the Multi Element Radio Linked Interferometry Network (MERLIN) array at 4.994 GHz with a bandwidth of 16 MHz. MERLIN is comprised of six individual antennas typically 25m in diameter and with a maximum separation of 217 km. Ten imaging runs were made as a target of opportunity program triggered by flux monitoring at the RT and GBI, showing the source had flared to around 250 mJy at 2–15 GHz. MERLIN, by default, samples both left hand and right hand polarisations allowing the full range of Stokes parameters to be imaged. Details of the observations can be found in the Table 1, and continuum and polarisation maps in Figs. 2 and 6 respectively.

Each separate epoch includes observations of a flux and polarisation angle calibrator, 3C286, a point source calibrator, OQ208 or 0552+398, the compact phase reference source, 1919+086 and the target GRS 1915+105. By nodding the array to the phase reference source, the interpolated phase variations due to atmospheric density variations were removed from the target source data. The nodding cycle of 8 minutes on the target and 2 minutes on the reference source reflects the phase stability of MERLIN at this frequency.

Phase referencing allows the registration of individual

MJD -50000.0	Total Flux Density	SE Posn.	Flux	M P/I	NW Posn.	Flux	M P/I	C1 Posn.	Flux	C2 Posn.	Flux	C3 Posn.	Flux	Typical Errors	
														Flux	Posn.
752.71	179.8	46	79.9	0.14	15	109.7	< 0.03							0.4	6
753.71	139.9	69	48.3	0.08	23	93.9	< 0.03							0.3	6
754.70	85.2	99	46.3	0.06	31	17.9	0.10	38	25.9					0.3	6
755.70	63.6	122	31.0	0.06	46	11.7	0.13	31	21.4					0.2	6
758.68	16.4	191	4.8		84	4.8		92	2.9	6	3.8			0.2	8
759.68	12.2	206	2.0		99	3.1		130	2.7	76	4.6			0.1	10
760.68	7.1	237	1.8		99	2.4				106	2.3			0.1	10
761.72	7.4	252	0.6		107	1.8		206	0.6	137	1.5	69	1.6	0.1	15
762.72	6.4	279	0.4		113	1.4		211	1.1	151	1.1	83	1.1	0.1	15
763.72	3.6	317	0.3		136	0.9		242	0.4	158	0.5	98	0.9	0.1	15

Table 1. Measured quantities from MERLIN maps: angular separation (mas) from the core, flux densities (mJy), and fraction of linear polarisation for all well-resolved components. SE and NW correspond to the approaching and receding components of the first major ejection. NW1 and NW2 correspond to the apparent splitting of component NW in the later epochs (see text). C1 – C3 are subsequent approaching ejections. M = P/I is the fractional linear polarisation, where measurable. The errors in fractional polarisation are typically 0.01 except for the last epoch quoted where they may reach 0.04 for the weaker NW component.

images to around 10 mas, given the changeable weather conditions during the observations. The absolute positions are tied to the radio reference frame (ICRF) using the calibrator 1919+086 whose position is known to around 17 mas relative to that frame (Patnaik et al 1992).

Using the MERLIN d-programs, initial data editing and amplitude calibration were performed and the data prepared for further reduction in the NRAO’s AIPS package. After further editing in AIPS, each dataset was run through the MERLIN pipeline, which images the phase reference source and applies the derived corrections. Instrumental polarisation corrections were made using 1919+086 and the polarisation position angles were calibrated using 3C286, for which a position angle of 33 degrees for the E vector of linear polarisation was assumed.

Subsequent self-calibration using the phase reference images as starting models was straight forward. Imaging the stokes parameters I, Q and U using the AIPS task IMAGR gives the final total intensity contour maps with superimposed vectors representing linearly polarised intensity. All the images have been restored with a 40 mas (FWHM) circular beam.

All the maps are affected to some degree by the variations in source structure and brightness during the observations. In 12 hours, the source expands by (typically) one-quarter of a beamwidth, and during the first 4 epochs the flux-density changes were as much as 10% over each individual epoch. Although these two effects are difficult to disentangle, and we are in the process of simulating such changes to quantify their magnitude, we believe that there will be no serious consequences for the images beyond increased uncertainties in the positions of components, at the level of a few mas, and the presence of sidelobes around bright components (at a few percent of the peak brightness) in the maps at early epochs.

Relative positions of components were found by measuring radial distances of the components from a nominal map centre. RMS errors in this process are estimated to be 6 mas, degrading to 15 mas for the weaker components in the later epochs. The error in the absolute position of each component is ~ 22 mas.

A montage of all ten epochs is presented in Fig. 2. At least four approaching (SE, C1, C2, C3) components and one receding (NW) component are clearly resolved. The receding component corresponding to ejection C1 may be also resolved in the last three epochs (less likely, but possible, is a physical splitting of component NW). The maps have been rotated clockwise by 52 degrees, so that the mean position angle of the jet on the sky is 142 degrees.

2.2 Ryle Telescope

The source was monitored at 15 GHz using the RT at Cambridge. At least a short observation was possible on most days during this period. The details of the observing technique are as given in PF97. The data, in 5-minute bins, are plotted in the top panel of Fig. 1. Data sampled at 32-sec intervals are shown in Fig. 7 for the rapid (oscillation) variations observed at four epochs.

2.3 Green Bank Interferometer

GRS1915+105 was monitored at 2.25 and 8.3 GHz throughout 1997 using the 2-element Green Bank Interferometer. The observing and calibration procedures were the same as described by Foster et al. (1996). Random errors for the GBI are flux density dependent, approximately (one sigma) 4 mJy at 2 GHz and 6 mJy at 8 GHz for fluxes < 100 mJy; 8 mJy at 2 GHz and 25 mJy at 8 GHz for fluxes near 0.5 Jy. We estimate that systematic errors may approach 10% at 2 GHz and >20% at 8 GHz. Fig. 1 displays the GBI data at 2 and 8 GHz during MJD 50700-50800 and exhibits both plateau (50730-50750) and flaring (50721-50725 and 50750-50756) behavior as described by Foster et al. (1996).

It should be noted that the *plateau* state discussed in this paper is consistent with the definition in Foster et al. (1996) but that our definition, i.e. flat spectrum radio emission at about 100 mJy at the same time as quasi-stable X-ray emission with a significant hardening of the spectrum, may be more specific.

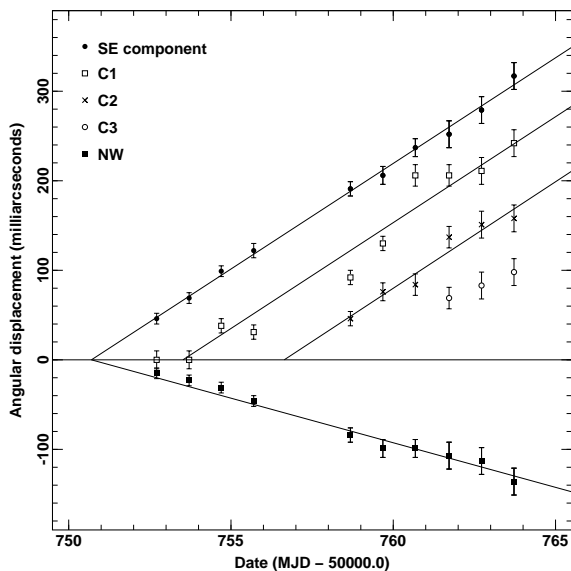


Figure 3. Angular separation as a function of time for approaching components SE, C1, C2 and C3 and receding component NW. All approaching components are consistent with unaccelerated proper motions of $23.6 \pm 0.5 \text{ mas d}^{-1}$, significantly faster than those reported in MR94. The receding component, NW, has a proper motion of $10.0 \pm 0.5 \text{ mas d}^{-1}$, and corresponds to the same ejection epoch as SE, on $\text{MJD } 50750.5^{+0.08}_{-0.2}$.

2.4 RXTE

The target is monitored up to several times daily in the 2–12 keV band by the Rossi X-ray Timing Explorer (RXTE) All-Sky Monitor (ASM). See e.g. Levine et al. (1996) for more details. The total flux measured by individual scans is plotted in the bottom panels of Figs. 1 and 7.

3 SUPERLUMINAL EJECTIONS

Fig. 2 presents the ten MERLIN maps of GRS 1915+105. The images clearly show expansion of the source, with components on the left-hand side (south east – maps have been rotated clockwise by 52 degrees) appearing to move faster. The two components just resolved in the first image can be followed through all epochs as they move out and their brightness declines. We label these components SE and NW. Further components can be seen to be ejected later and are labelled C1, C2 and C3. The proper motions of the components are consistent with ballistic motions, and so we can extrapolate back to derive their times of formation (see Fig 3). We estimate these to be as follows (in MJD):

$$\text{NW} + \text{SE} : 50750.5^{+0.08}_{-0.2}$$

$$\text{C1} : 50753.5 \pm 0.8$$

$$\text{C2} : 50756.6 \pm 1.6$$

$$\text{C3} : 50758.0 \pm 2.0$$

The latest time of the NW+SE ejection is constrained by the observation of core-dominated radio oscillations by MJD

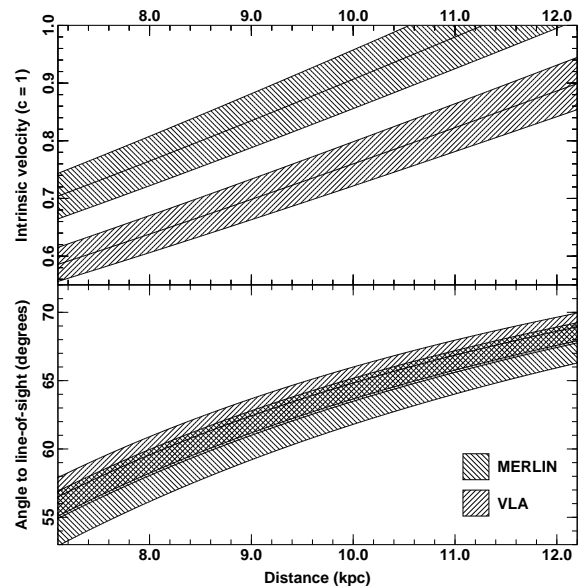


Figure 4. Derived intrinsic velocities and angles to the line-of-sight for MERLIN and VLA observations, under the assumption of intrinsically symmetric ejections. Solutions are possible for the same angle to the line-of-sight during both sets of observations, but the velocity derived for the MERLIN observations is **higher** than that for the VLA observations, by $\Delta\beta \sim 0.1$.

50750.58 (Fig. 7), as well as uncertainties in the model fits. The individual components are unresolved in the first 4 epochs. There is some evidence of them becoming resolved or breaking up into sub-components in the latest 3 epochs. Epochs 5, 6, 7 and 9 show that there is some emission between the knots which may indicate the presence of an underlying continuous jet. However, given the possible problems of varying flux density and structure through the observations and the low signal-to-noise ratio in the later epochs, we cannot be certain about some of these features. The possible bending of the jet will be discussed briefly below.

We will concentrate our quantitative analysis on those components which can be followed through 3 or more epochs. The rapidly outflowing components are generally moving faster, and brighter, on the SE side. (Note that the apparent high brightness of the NW component in the second epoch is due to a blend with the core).

From these components we can measure proper motions, flux densities and (in some cases) polarisations. These we deal with quantitatively below.

3.1 Proper motions

An examination of the positions of the components shows an apparent expansion velocity at greater than $2c$, thus relativistic effects are important. As a result the approaching components will have a higher apparent motion than that of the receding components. The component to the NW clearly has the lowest apparent speed we therefore identify it as receding; there are 3 components to the SE which we identify as approaching. The data are best fit by proper motions of

$$\mu_{\text{app}} = 23.6 \pm 0.5 \text{ mas d}^{-1}$$

and

$$\mu_{\text{rec}} = 10.0 \pm 0.5 \text{ mas d}^{-1}$$

All fits are good, with $\chi_{\text{red}}^2 \leq 1$, and illustrated in Fig. 3. The proper motion of $17.6 \pm 0.4 \text{ mas d}^{-1}$ reported by MR94 for the approaching component can be ruled out; fixing the proper motion to this value does not give an acceptable fit to the data.

Following the method of MR94, *under the assumption of an intrinsically symmetric ejection*, we can derive

$$\beta \cos \theta = \frac{\mu_{\text{app}} - \mu_{\text{rec}}}{\mu_{\text{app}} + \mu_{\text{rec}}} = 0.41 \pm 0.02, \quad (1)$$

where β is the velocity of the ejections expressed as a fraction of the speed of light, and θ is the angle between the ejection and the line-of-sight. This immediately gives us a maximum angle to the line-of-sight (setting $\beta = 1$) of $\theta_{\text{max}} \leq 66 \pm 2^\circ$, and a minimum velocity (setting $\cos \theta = 1$) of $\beta_{\text{min}} \geq 0.41 \pm 0.02$.

A maximum distance to GRS 1915+105 can also be inferred for a maximum possible velocity of the ejecta of $\beta = 1$

$$d_{\text{max}} \leq \frac{c \tan \theta_{\text{max}} (\mu_{\text{app}} - \mu_{\text{rec}})}{2 \mu_{\text{app}} \mu_{\text{rec}}} \quad (2)$$

which can be expressed in convenient units as

$$d_{\text{max}} \leq 87 \tan \theta_{\text{max}} \left(\frac{\mu_{\text{app}} - \mu_{\text{rec}}}{\mu_{\text{app}} \mu_{\text{rec}}} \right) \text{ kpc} \quad (3)$$

(for μ_{app} and μ_{rec} in mas d^{-1}). The proper motions observed with MERLIN therefore constrain the maximum distance to be $11.2 \pm 0.8 \text{ kpc}$. MR94 state that GRS 1915+105 must be further than the HII region G45.45+0.06 (mistyped by them as G45.46+0.06; Downes et al. 1980) based upon their HI spectral observations. While MR94 state that this HII region lies at $\sim 8.8 \text{ kpc}$, in a recent study Feldt et al. (1998) adopt a distance of 6.6 kpc , and so GRS 1915+105 appears to lie at a distance of between $7 - 12 \text{ kpc}$, significantly closer than previously thought. Given the high observed HI column density to the source, from which MR94 inferred a large distance of $12.5 \pm 1.5 \text{ kpc}$, we adopt a value of 11 kpc for the distance to GRS 1915+105.

We can solve for the angle to line-of-sight and velocity, for any distance to GRS 1915+105. The angle to the line-of-sight

$$\theta = \tan^{-1} \left[1.16 \times 10^{-2} \left(\frac{\mu_{\text{app}} \mu_{\text{rec}}}{\mu_{\text{app}} - \mu_{\text{rec}}} \right) d \right], \quad (4)$$

where d is the distance to the source in kpc, and μ_{app} and μ_{rec} are in mas d^{-1} . Once θ is calculated, we can immediately derive β as the value of $\beta \cos \theta$ is already known.

Table 2 lists the apparent velocities and solutions for the angle to the line-of-sight and intrinsic velocities for both these MERLIN observations and the VLA observations of MR94, for assumed distances of 9, 10, 11 & 12 kpc. Fig. 4 shows these solutions for all distances between $7 - 12 \text{ kpc}$. Our MERLIN data unequivocally imply a higher intrinsic velocity, by $\Delta\beta \sim 0.1$, in comparison to the observations reported in MR94.

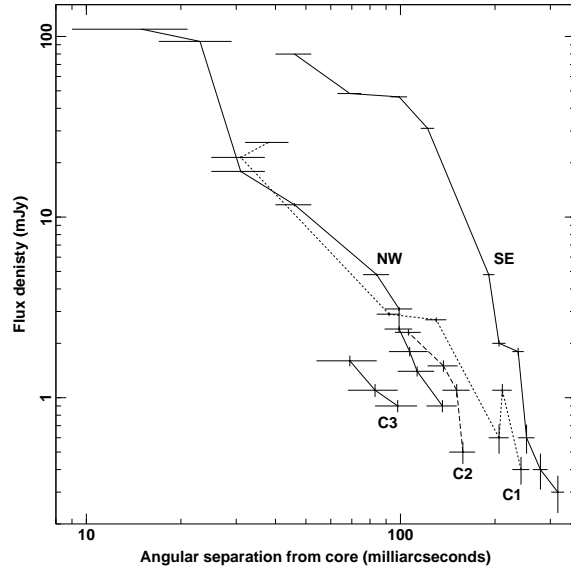


Figure 5. Flux densities of individually-resolved components as a function of angular separation from the core. Simple power-law and exponential decay models do not fit the data well. The flux density ratio of SE : NW, approaching and receding components from the same ejection, ranges from 6 – 10.

3.2 Flux densities and ratios

The ratio of flux densities from the approaching and receding components is another important diagnostic of the ejections. In the above calculations we have assumed geometric symmetry; here we also assume that the jet components on both sides have the same intrinsic luminosity (which does not appear to be the case for GRO J1655-40; Hjellming & Rupen 1995). When measured at equal angular separations from the core (i.e. the same time since ejection in the rest frame of the ejecta) and coupled with the observed spectral index we can test the theoretical predictions for Doppler (de-)boosting of the components.

The mean spectral index of the ejecta is hard to determine due to both overlapping ejection events and the presence of rapid flat-spectrum oscillations from the core (PF97 and below). Our best estimate for the index, defined as $\alpha = \Delta \log S_\nu / \Delta \log \nu$ is around -0.8 , the same as reported by MR94. This is determined primarily from the simultaneous Green Bank monitoring at 13.3 and 3.6 cm and should be a good estimate for the 6 cm MERLIN observations. It is difficult to measure accurately the ratio of flux densities of the components at equal angular separations, given their very different proper motions, but it lies between 6 and 10. This is compatible with the 8 ± 1 reported in MR94.

For bulk motions at velocity β the observed ratio is predicted to be

$$\frac{S_{\text{app}}}{S_{\text{rec}}} = \left(\frac{1 + \beta \cos \theta}{1 - \beta \cos \theta} \right)^{k-\alpha}, \quad (5)$$

where, theoretically, $k = 2$ for continuous jets and 3 for discrete components. As $\beta \cos \theta$ is already calculated as 0.41 ± 0.02 , and independent of distance, we can solve for

Distance (kpc)	Apparent velocity				Angle to line-of-sight		Intrinsic velocity		Bulk motion Lorentz factor	
	(appr.)		(reced.)		MERLIN	VLA	MERLIN	VLA	MERLIN	VLA
9	1.2c	0.93c	0.53c	0.48c	62°	63°	0.84c	0.71c	1.8	1.4
10	1.4c	1.1c	0.59c	0.55c	64°	66°	0.92c	0.79c	2.6	1.6
11	1.5c	1.2c	0.64c	0.60c	66°	68°	0.98c	0.86c	5.0	2.0
12	1.5c	1.2c	0.66c	0.63c	68°	69°	1.01c	0.89c	–	2.2

Table 2. Apparent velocities, solutions for the angle to the line-of-site, intrinsic velocity of ejection (assuming symmetry), and bulk motion Lorentz factors for values of proper motion measured by MERLIN and previously by the VLA (MR94), for assumed distances of 9, 10, 11 and 12 kpc. The functions are plotted in full, with consideration of measurement errors, in Fig. 4

k . For a flux density ratio of in the range 6 – 10, $k = 1.3$ – 1.9. As in MR94, the flux ratio appears to be closer to that expected for a continuous jet than for discrete components (although the value derived from the data of MR94 is $k = 2.3$, interpreted by them as implying something intermediate between a continuous jet and discrete ejections). For $k = 3$ we would have expected a flux ratio of ~ 27 .

Fig. 5 shows the flux density of each well-observed component as a function of angular separation from the core. As is obvious from Table 1 and the maps of Fig. 2, the ejections in the sequence NW+SE, C1, C2, C3 are of steadily decreasing flux density. While uncertainties in both flux density and position make interpretation difficult, the data do not appear to show the straight line behaviour expected for a power-law decay (for the case of adiabatic expansion losses and a constant expansion rate). Exponential fits to the data provide no improvement. RM99 discuss a steepening of the decay of the radio flux density at an angular separation of ~ 1 arcsec; as we only image on smaller scales we cannot test this. Atoyan & Aharonian (1997) discuss the implications of the flux ratio in considerable detail.

3.3 Polarisation

Polarisation images have been made for the first four epochs, when the source was sufficiently bright to detect linear polarisation at the level of a few percent. These are shown in Fig. 6, where the vectors represent the fractional linear polarisation and observed electric field angle. The fractional linear polarisations are also listed in Table 1. No circular polarisation was detected at any time, with a conservative upper limit of 2%.

3.3.1 Resolved ejecta

The images of the ejected components show a striking asymmetry in the linear polarisation – only the approaching SE component appears significantly polarized. Its fractional polarisation decreases rapidly from 14% to 6%, and the polarisation position angle swings by approximately 75 degrees between the second and third epochs, then swings back by 45 degrees. In the fourth epoch image, there is marginal detection of polarized emission in the receding NW component, at a level of $13 \pm 5\%$.

The changes in polarisation seen in the MERLIN images could be a result of changing Faraday effects (internal or external) or changing magnetic field geometry within the radio components. With only a single frequency it is hard

to distinguish between these possibilities. If the observed change in position angle is due to Faraday rotation, the implied change in rotation measure is $> 300 \text{ rad m}^{-2}$.

The radio components are believed to be considerably denser than their surroundings (observed limits on the deceleration imply a density contrast of at least 10) and have equipartition field strengths of order 50 mG (see below), presumably much greater than in the surrounding medium. The Faraday depth, or rotation measure, is proportional to $nB(Ld)^{1/2}$, where n is the thermal electron density, B is the magnetic field strength, L is the path length and d is the field tangling scale. The Faraday depth within the source is therefore likely to exceed the Faraday depth of a surrounding medium distributed on a scale size comparable to the source itself. As the components expand their internal Faraday depths will fall, and any internal Faraday depolarisation would decrease. This is contrary to the observed decrease in fractional polarisation. Therefore, we do not believe the changes in polarisation are due to changing Faraday depths, and this is consistent with the low rotation measure observed by Rodríguez et al. (1995).

Rodríguez et al. (1995) noted a fractional polarisation of approximately 2% at 5.0, 8.4 and 15 GHz at a position angle of 178 ± 10 degrees on 24 March 1994, when the source was barely resolved by the VLA and 5 days after the radio components were ejected. At this time the emission was probably dominated by the approaching component. The similarity of the fractional polarisation and position angle at the three wavelengths implies that Faraday effects were small at 5.0 GHz. The implied upper limit to the Faraday rotation measure is 50 rad m^{-2} .

Superluminal jets in AGN often show complex radio polarisation behaviour: rapid variations in polarisation position angle (e.g. 0917+624 for an extreme case, Quirrenbach et al. 1989) and small-scale variations along the jet (e.g. 3C454.3, Kemball, Diamond & Pauliny-Toth 1996). This is usually interpreted as being due to shocks, which compress and order the magnetic field (Cawthorne et al. 1993), and which appear as radio knots in an otherwise continuous jets.

The radio components of GRS1915+105, on the other hand, are thought to be discrete plasmons, rather than features (shocks or otherwise) in a continuous jet. In this case the changes in radio polarisation indicate changes in the internal magnetic field geometry, such as randomization of the magnetic field as the plasmons evolve. The effects of aberration on a planar structure such as a shock would result in the two components having different observed polarisation characteristics. However the low signal to noise for the mea-

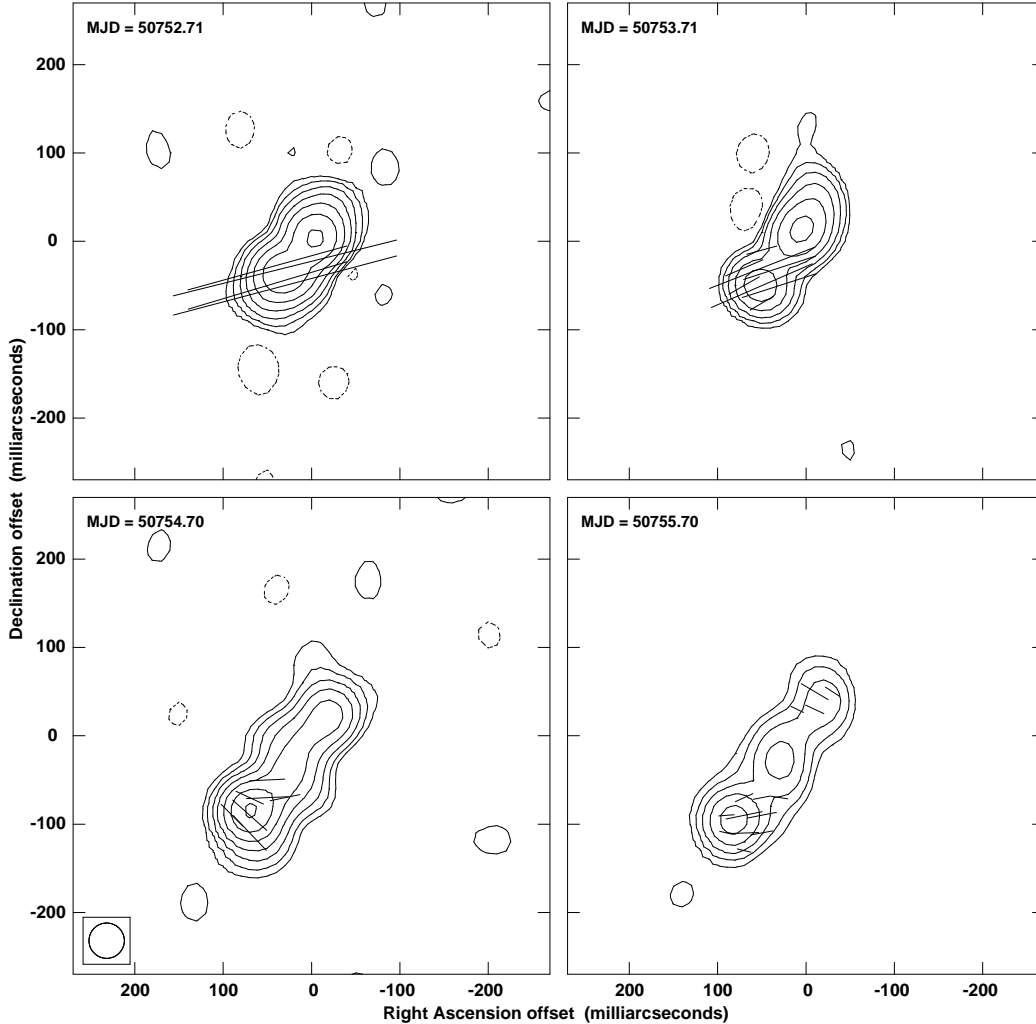


Figure 6. Linear polarisation E vectors superimposed upon total intensity contour maps of the first four epochs of MERLIN observations. For polarisation vectors, 100 mas = 3.33 mJy/beam. This clearly shows the depolarisation of the core and receding components with respect to the approaching component, and the rotation of polarisation vectors in the approaching component.

surement of polarisation in the receding component does not allow us to make such a distinction in this case.

3.3.2 Core

The core, sometimes blended in our images with newly formed major ejections, does not at any time show significant linear polarisation. In particular, during the first two epochs of observation, the core is dominated by the flat spectrum oscillations of the type discussed in detail in PF97 (see Fig. 7). The lack of observed polarisation may be due to superposition of multiple components with different polarisation position angles within the beam, or large Faraday depths close to the binary system (either internal to the compact base of the jet or in the form of circumstellar material).

3.4 An underlying curved jet ?

In several of the MERLIN maps there is a hint of extended emission between the components. Furthermore, the low value of k derived from the flux density ratios and $\beta \cos \theta$ is more consistent with a continuous jet than physically discrete components (see above). In addition, the jet appears to be curved, an effect which may also be marginally apparent in reinspection of the VLA images of MR94.

Firstly, comparing the flux in discrete components in the MERLIN maps with respect to radio monitoring with GBI and RT (in which the source and jets will be unresolved), we find that the values agree to within a few per cent. So the overwhelming majority of the synchrotron emission, at cm wavelengths at least, arises in unresolved (with MERLIN) bright spots. On the other hand, we both derive (section 3.2) and apply (section 4.1) $k \sim 2$, the value theoretically expected for a continuous jet. We must conclude that the data are not good enough at present to definitively establish whether the ejections are in discrete components or we are observing the bright parts of a continuous jet. In

the latter case we can at least now state that any underlying continuous jet is very faint and less than a few mJy at cm wavelengths

The possible curvature of the jet is not addressed quantitatively here, but we do believe this effect to be real. Discrimination between ballistic and helical effects, the latter possibly due to Kelvin-Helmholtz instabilities, is not possible at this stage. The ‘period’ of any bending observed at angular scales imaged with MERLIN is around 7 days. It is interesting to note that the ‘period’ of the jet bending in GRO J1655–40 reported by Hjellming & Rupen (1995) of 3.0 ± 0.2 d turned out to be very close to the subsequently discovered orbital period of 2.6 d (Bailyn et al. 1995). We are confident that the apparent bending is not due to the rapid angular and flux density evolution of the source during a 12-hr observation (c.f. however, VLBI observations of GRO J1655–40, Tingay et al. 1995, where both higher proper motions and finer angular resolution exacerbated the effect).

3.5 Collimation and expansion of components

From the lack of clearly resolved structure perpendicular to the jet axis at the 40 mas resolution of MERLIN, we can place constraints on the opening angle and lateral expansion of the ejected components. The maximum distance from the core that we track ejected components is ~ 300 mas, and this constrains the opening angle of the jet to ≤ 8 degrees over distances from the core ≤ 4000 A.U. (6×10^{16} cm). Similarly the ratio of lateral expansion to forward velocities is constrained to be ≤ 0.14 , i.e. a maximum lateral expansion velocity $\leq 0.14c$ (for jet bulk velocity of c).

4 DISCUSSION

4.1 Energetics and mass flow

4.1.1 Estimation of the internal energies of the jet components

Initially, we must work in the rest-frame of the emission region. Converting the observed parameters (emission frequency, luminosity etc) requires the value of the bulk Lorentz factor γ , which is somewhat uncertain as discussed in section 3.1, on account of the uncertainty in the distance. Because of the large angle to the line-of-sight, the Doppler factors for both the approaching and receding components,

$$\delta_{\text{app,rec}} = \gamma^{-1}(1 \mp \beta \cos \theta)^{-1} \quad (6)$$

are both less than unity for the range of Lorentz factors considered here.

The estimation of the parameters of the synchrotron emission region is detailed by Longair (1994) and Hughes (1991). We adopt the formulae in the summary by Longair (allowing for the opposite convention for the sign of α). These include a number of simplifying assumptions which are unlikely to introduce larger uncertainties than those imposed by our imperfect knowledge of the source parameters.

In order to estimate the internal energy of the emitting component, we need to know the synchrotron spectrum and the source geometry. A radio spectrum of the form $S \propto \nu^\alpha$ arises from an electron population with an energy spectrum $N(E) \propto E^{-(1-2\alpha)}$. The observed luminosity can arise from

various combinations of magnetic flux density B and particle density, both of which we assume to be spatially uniform; the total energy is minimised to derive the “minimum energy” conditions: the total energy in relativistic electrons, and the misleadingly-named B_{min} , the field at which the total energy is minimised. As is well known, the minimum energy result nearly coincides with equal energies in magnetic field and particles, or equipartition. There are physical plausibility arguments for such a situation, but very few measurements which confirm that this situation might actually pertain in any particular case (see Harris, Carilli & Perley 1994 for data on the radio galaxy Cygnus A which suggest, in that case, that conditions may be near to those suggested by this method).

The calculation can easily be adapted to include a contribution to the energy by a hypothetical population of relativistic protons, which do not radiate significantly by the synchrotron mechanism if their energies are comparable with those of the electrons.

If the energy spectrum of the electrons is relatively steep (α steeper than -0.5), as in this case, the total energy of the particles is dominated by the lower end of the distribution. The lowest frequency detected, and the luminosity at that frequency, are then parameters in the calculations.

The source geometry is, so far, not well-defined. Direct observations only give an upper limit to most dimensions: the resolution of MERLIN is 50 mas, corresponding to 8×10^{13} m, or 3 light days, at 11 kpc. We have to rely on the time-scale of the variations in flux density for a better limit; the rise times are the shorter and therefore more restrictive. The rise time may represent the interval during which relativistic material is injected, or alternatively a transition in optical depth (or both). We believe that the former (injection timescale) is more probably the dominant effect, since the spectral data suggest that the source is optically thin as soon as the jet is visible.

Since the rise-time for the jet components appears to be less than 12h, we adopt 12 light-h (1.3×10^{13} m) as a “typical” size on formation of the jet component. In comparison, RM99 discuss a geometric mean angular size of 35 mas, corresponding to a linear scale of 6×10^{13} m. We stress the weak links in this argument, elaborated by Longair (1994) and by Hughes (1991):

- We have only rather weak constraints on the source size, and certainly do not know the filling factor of the source, and this is one of the major uncertainties in the calculation. A smaller size or filling factor reduces the total energy required as $(\text{volume})^{3/7}$.
- There is little evidence that the minimum-energy condition is achieved.
- The contribution of protons (and other nuclei) is not known.
- The limits on the energy spectrum are not well-defined by current observations.

We now apply the formulae from Longair (1994); his equations 19.29 and 19.30, using the following measured, estimated or derived parameters:

- (i) adopted distance 11 kpc
- (ii) $\gamma = 5.0$ (see Table 2)
- (iii) $\beta \cos \theta = 0.41$

Table 3. A summary of the derived properties of the ejecta at minimum energy conditions, calculated for a distance of 11 kpc, and summing both sides of the ejection. We assume that radio emission observed by GBI and RT at the peak of the flare are dominated by the approaching (SE) component, and take 1 and 15 GHz as upper and lower bounds of the observed flaring emission respectively. We assume a generation time for the ejection of 12 hr. Proton mass and mass flow rate are for the case of 1 proton for each electron.

Minimum energy condition			N_e	Ejecta		Power (erg s ⁻¹)	Mass outflow rate (g s ⁻¹)
E_{\min} (erg)	$E_{K,\min}$	B_{\min} (mG)		$M_e(\text{rest})$ (g)	M_p (g)		
2×10^{43}	2×10^{44}	280	3×10^{46}	3×10^{19}	5×10^{22}	2×10^{39}	10^{18}

- (iv) spectral index $\alpha = -0.8$
- (v) Doppler factors $\delta_{\text{app,rec}} = \gamma^{-1}(1 \mp \beta \cos \theta)^{-1} = 0.34, 0.14$
- (vi) $k = 2$ (section 3.2)
- (vii) ratio of relativistic proton energy to electron energy, $(\eta - 1) = 0$
- (viii) total source volume $V = 10^{39} \text{ m}^3$
- (ix) monochromatic luminosity L_ν in the rest frame, at the lowest frequency detected, as derived below.

The maximum observed flux density observed at the start of the outburst at 2.3 GHz is 550 mJy (Fig 7), some 2 days before the first MERLIN map. This would correspond to 1 Jy at 1 GHz, assuming the spectral index to be -0.8 . We adopt 1 GHz as the lowest frequency at which emission was detected during this outburst (Hannikainen & Hunstead, private communication, detected the outburst at 843 MHz). We assume that this flux density is dominated by the approaching component. Its apparent flux density if observed in its rest frame would be about 20 Jy; signals received at 1 GHz would have been emitted at $\nu = 3$ GHz, and the luminosity $L_\nu = 2.9 \times 10^{17} \text{ W Hz}^{-1}$.

The minimum total energy is

$$W_{\min} \simeq 3.0 \times 10^6 \eta^{4/7} (V/\text{m}^3)^{3/7} (\nu/\text{Hz})^{2/7} (L_\nu/\text{W Hz}^{-1})^{4/7} \text{ J} \quad (7)$$

and the associated magnetic field is

$$B_{\min} \simeq 1.8 (\eta (L_\nu/\text{W Hz}^{-1}) / (V/\text{m}^3))^{2/7} (\nu/\text{Hz})^{1/7} \text{ T} \quad (8)$$

This set of parameters, for one of the radio-emitting components, leads to $W_{\min} = 7.7 \times 10^{35} \text{ J} = 7.7 \times 10^{42} \text{ erg}$ and $B_{\min} = 28 \mu\text{T} = 280 \text{ mG}$.

The Lorentz factor of an electron radiating near 3 GHz is then about 90, and the mean Lorentz factor for this population is 240. (Some authors consider electron distributions which continue to much lower energies, but as yet there is no observational evidence for this. RM99, on the other hand, adopt a higher mean Lorentz factor of 1000, on the basis of a detection of the event at 240 GHz. That emission may well have originated in the inner region of the system; Fig 7 shows the quasi-periodic oscillations observed at 15 GHz during the early stage of the current outburst which have a flat spectrum (Fender & Pooley 1998) and, with a time-scale of 20 min, must come from a very small region.)

4.1.2 Total number of relativistic electrons

By integrating the electron distribution we can derive an estimate of the total number of relativistic electrons (this may become important if we suppose that each is accompanied by a ‘‘cold’’ proton). This integration requires minimum and maximum energies, but as in the derivation of the total energy the precise value of the upper limit is unimportant;

the number is dominated by the low-energy electrons. To establish the constants involved we use equation 19.17 from Longair, which relates the luminosity, the magnetic field and the spectrum, and derive

$$N_{\text{total}} = (L_\nu/\text{W Hz}^{-1})f(\alpha)/(B_{\min}/\text{T})$$

where $f(\alpha) = 1.7 \times 10^{24}$ for $\alpha = -0.8$. This results in $N_{\text{total}} = 1.6 \times 10^{46}$.

4.1.3 Kinetic energy

Associated with the bulk motion of the jet there is also the kinetic energy; if the jet contains only e^+e^- plasma and magnetic field, the magnitude of this is $(\gamma - 1) \times W_{\min}$, perhaps $9 \times 10^{36} \text{ J} = 9 \times 10^{43} \text{ erg}$. On the other hand, if the plasma contains cold protons, the kinetic energy will be increased by $(\gamma - 1) \times N_{\text{total}} m_p c^2$. This results in an increase of only a factor 2. The total of the kinetic energy of the protons could vary, either way, if the conditions were far from ‘‘minimum energy’’, or be substantially larger if the electron energy distribution continues to rise to lower energies, with correspondingly more protons.

We can estimate the power required to produce this injection of energy over 12 h; including the kinetic energy of the system and both sides of the source, we have to generate $2 \times \gamma W_{\min}$ in that time, a power of $2 \times 10^{32} \text{ W}$ or $2 \times 10^{39} \text{ erg s}^{-1}$. Including a similar number of protons approximately doubles that total and also requires a mass-flow rate of $\geq 10^{18} \text{ g s}^{-1}$. X-ray spectral fits (e.g. Belloni et al. 1997b) have been used to derive accretion rates near 10^{18} g s^{-1} .

Many of the observed parameters used here are uncertain, with the dominant effect arising from the unknown distance. Were we to adopt a distance of 9 kpc, the bulk Lorentz factor would be 1.8 rather than 5 and the Doppler factor of the approaching component near 1. Therefore its flux density in the rest frame would be 1 Jy rather than 20 Jy, and the energy of the system reduced by a factor of about 10.

The results of these calculations of energetics and mass flow are summarised in table 3 (for a distance of 11 kpc). Indeed the mass of cold protons could be as much again as in table 3 if we use the upper limit on electron density ($< 2 \text{ cm}^{-3}$) inferred from Faraday effects discussed in section 3.3.1.

4.2 Comparison with previous major ejections

While it could already be guessed from the higher observed proper motions, our solutions (Table 2, Fig. 4, under the assumption of intrinsic symmetry) illustrate that we cannot

avoid deriving a higher velocity for the ejecta than derived by MR94. Thus the two data sets are *not* compatible with a simple change of the angle to the line-of-sight of a jet which is intrinsically physically identical. In fact the data *are* marginally consistent with the *same* angle to the line of sight for the jet. The increase in intrinsic β from our observations compared to MR94 is at least 0.05, and more likely ~ 0.1 , corresponding to a significantly higher Lorentz factor for bulk motion by a factor of ≥ 1.3 , as tabulated in Table 2.

It is of great importance to determine whether the different measured velocities are intrinsic to the ejecta or an artefact of the different resolutions of MERLIN and the VLA. In the former case the significantly different measured proper motions could correspond to a difference between the ejection event(s) reported here and the event reported in MR94. The earlier event appears to have been both significantly brighter and to have decayed in flux more slowly. Alternatively, there may be genuine deceleration between the angular scales of up to 300 mas imaged with MERLIN and greater than 400 mas measured with the VLA. This does not seem likely however, given that both instruments recorded essentially ballistic motions (ignoring the slight apparent curvature) within their multiple observations.

It may be that the different measured proper motions arise from an inability of the VLA to resolve individual components, causing them to blend together in maps. In this case, the VLA could measure lower proper motions and/or apparent decelerations if

- (1) There were multiple components, and
- (2) The components decreased in flux density more rapidly with distance from the core.

This effect is discussed by Hjellming & Rupen (1995) for GRO J1655–40 where they measure apparent decelerations of $\sim 30\%$ with the VLA in comparison to VLBA (and SHEVE – Tingay et al. 1995) for two of the three major ejections that they image. Did these effects occur during the observations of MR94? Their maps do indeed show that multiple ejections were occurring during this period (MR94; RM99); and furthermore RM99 discuss evidence that the decay rate of the ejecta increase with angular separation from the core (although they discuss a relatively abrupt increase in decay rate at angular separations ≥ 1 arcsec, which would not have affected the measurements of MR94). So it seems a possibility that the lower measured proper motions arise from blending of multiple components and that the MERLIN measurements more accurately represent the true situation.

In order to test this we have attempted to convolve our MERLIN data with lower-resolution beams comparable to that of the VLA observations of MR94. Note that the comparison is not good because of the lack of short baselines in the MERLIN array compared to the VLA. Nevertheless, it was clear from convolution of our data with a 250 mas beam that it was not possible to clearly resolve any individual components. Even with a 100 mas beam, i.e. twice the resolution of the VLA data of MR94, while the approaching and receding sides can be distinguished, individual ejecta on the approaching side cannot.

However, without simultaneous VLA and MERLIN (and possibly also VLBI) observations of the outburst, it

is not possible to test this conclusively. So we cannot confidently discriminate between the two most likely explanations, of either intrinsically different velocities between March/April 1994 and Oct/Nov 1997, or resolution effects between the two arrays. Note that if the latter is the cause of the different measured proper motions then it requires the similar proper motions (range 15 – 18 mas d⁻¹) measured in four instances in 1994 with the VLA (RM99) all to have an origin in similar unresolved multiple ejections. Detailed inspection of radio light curves around these periods may shed some light on this.

The mean position angle of the jet as observed by MERLIN, 142 degrees, is consistent with the range of 140 – 160 degrees observed with the VLA (RM99).

4.3 X-ray and radio state at jet formation

GRS 1915+105 offers a unique opportunity to study the jet – disc relation, and in this case we can directly relate changes in the accretion disc X-ray emission to the ejection of significant quantities of material from the system.

Fig. 1 shows the evolving sequence of events as observed by radio and X-ray monitoring of the source. The onset of the plateau phase is preceded by a significant radio flare, similar enough to those mapped by us after the plateau state to interpret it as a major disc ejection.

Almost immediately following this ejection the plateau state is established. It was already known from PF97 that this state, with hard, quasi-steady X-ray emission, corresponded to bright and fairly steady radio emission at 15 GHz. Combination of the RT and GBI data now clearly show that this state is indeed radio bright, with a flat or inverted spectral index. This is highly indicative of absorbed emission (although it is conceivable that the electron acceleration mechanism changes to produce a different, optically thin, spectrum which mimics absorption), and may suggest the formation of a large optically thick jet. If so, it seems possible that this may be associated with the infrared jet imaged by Sams, Eckart & Sunyaev (1996). The X-ray emission may also support such a picture, as the soft (disc) component appears to be very weak, if present at all, during this state (Mendez & Belloni, private communication). In addition, no radio oscillations, associated with inner disc instabilities, have been observed during the plateau state.

Fig. 7 shows in more detail the radio and X-ray state of the source at the times of formation of the jets we have imaged with MERLIN. In particular note the four panels on the right hand side of Fig. 7, showing the 15-GHz RT monitoring of GRS 1915+105 between MJD 50750 and 50754, i.e. between the first ejection, corresponding to NW+SE, and the second, corresponding to C1. It appears that for the entire period between these two ejections, the inner accretion disc is unstable and material is repeatedly advected and ejected on timescales of tens of minutes (see Belloni et al. 1997a,b; Fender et al. 1997; PF97; Eikenberry et al. 1998; Mirabel et al. 1998; Fender & Pooley 1998). No such periods of large amplitude inner disc instabilities are obvious between subsequent ejections, although the ejection of C2 appears to correspond to a minor X-ray flare, and C3 possibly corresponds to a brief X-ray dip.

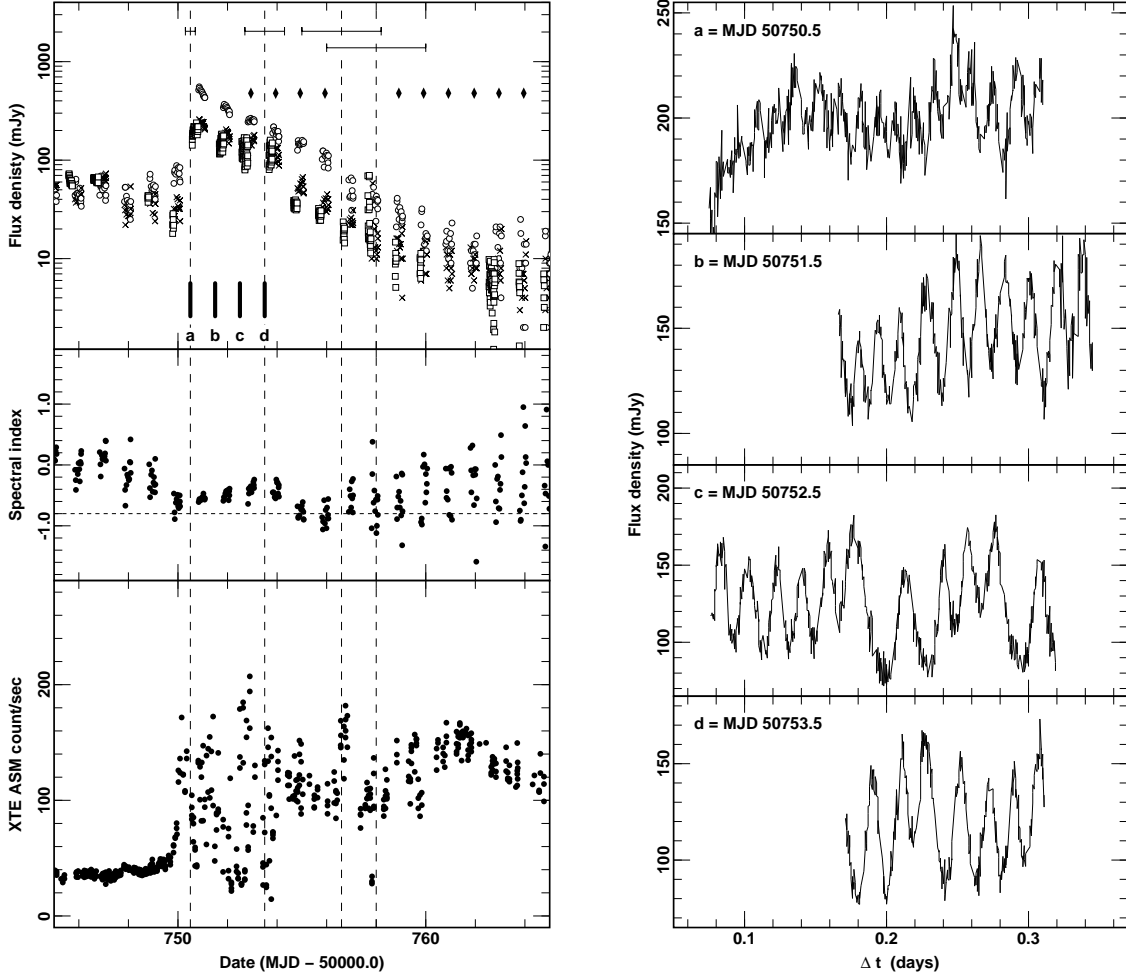


Figure 7. A detailed view of the radio and X-ray behaviour of GRS 1915+105 during the ejection episode. Symbols are as shown in Fig. 1. The vertical dotted lines, with error bars, indicate our derived times for the beginning of each of the four ejections. The four solid vertical bars labelled **a** – **d** drawn on the top left radio monitoring panel between the first and second ejections, indicate the four periods of 15-GHz monitoring highlighted in the panels on the right. The source appears to exhibit continuous short period (20–40 min) oscillations in this phase, indicative of repeated advection or ejection and refill of the inner accretion disc. The radio QPO do not repeat after the second ejection, but there are some indicators of the second and third ejections in the X-ray data.

5 CONCLUSIONS

Our MERLIN observations have revealed four major relativistic ejections from GRS 1915+105 over a period of approximately two weeks. Over ten epochs of observation we have consistently measured proper motions of 23.6 ± 0.5 and 10.0 ± 0.5 mas d^{-1} , for the approaching and receding components respectively. The proper motion of the approaching component is more than 30% higher than that reported from VLA observations of the source (MR94; RM99). Under the assumption of intrinsic symmetry, we have derived an upper limit for the distance to the system of 11.2 ± 0.8 kpc. While compatible with the distance of 12.5 ± 1.5 kpc quoted by MR94, it seems that the favoured distance to the system should be revised downwards by at least 1 kpc. Solving for angle to the line-of-sight and intrinsic velocity, again under the assumption of an intrinsically symmetric ejection, we cannot avoid deriving a significantly higher velocity than MR94, by around $\Delta\beta = 0.1$. We have investi-

gated whether or not the lower resolution of the VLA could result in lower proper motions being measured, as a result of multiple blended components and an increase in decay rate with distance from the core, and this does seem possible. On the other hand, there is no reason to believe that the jet velocity should be fixed – of all the astrophysical objects with relativistic jets, only SS 433 (jet velocity $0.26c$, e.g. Vermeulen et al. 1993) is established to have a constant jet velocity. Further observations at high angular resolutions with MERLIN and/or VLBI, preferably simultaneous with lower resolution VLA observations, will be required to investigate whether there is a systematic deceleration of ejecta on angular scales of ≥ 0.3 arcsec. If MR94 are correct in inferring a large distance for GRS 1915+105 from the column density to the source, then the bulk velocity of the outflow is almost certainly much higher than the currently accepted value of $0.92c$; at 11 kpc we derive $0.98^{+0.02}_{-0.05}c$ at 66 ± 2 degrees to the line-of-sight.

Our polarisation observations clearly reveal rapid evo-

lution of the magnetic field in the ejecta on timescales of a day or less. This would seem to imply that the region from which the polarised emission arises is smaller than one light day across; consideration of time dilation (stretching intrinsic timescales when observed in our frame, given our derived solutions for θ and β) only makes this size smaller. The decreasing trend of the polarisation with distance from the core suggests increasing randomisation of the field as the ejecta evolve, although multi-frequency polarisation measurements are required to rule out or constrain Faraday rotation effects.

As already noted by MR94 and others, the power required for the formation of the jet is immense, far greater than the Eddington luminosity for a solar mass object (at 11 kpc), even without the inclusion of a proton content. Jet formation may well be the dominant power output channel during such periods, and possibly also during periods of smaller oscillation ejections. In addition, when one proton per electron is added the minimum mass flow rate becomes comparable to the mass accretion rates derived from X-ray spectral fits. So, it is possible that during jet formation periods a significant fraction of the inflowing mass is expelled and does not fall into the black hole. A similar possibility exists for the minor oscillation ejections (Fender & Pooley 1998). Good wavelength coverage of flares to both higher and lower frequencies is required to better determine the luminosity, energy and mass of the ejections. An accurate simultaneous comparison of mass flow through the disc (from X-ray spectral fits) and outflow rates (from radio observations) would be of great interest, to see whether the flows are advection- or ejection-dominated.

Radio and X-ray monitoring of GRS 1915+105 (e.g. Harmon et al. 1997; PF97) had already hinted at a delayed relation between hard X-ray states and radio outbursts. These MERLIN observations have established that these radio outbursts do indeed correspond to relativistic ejections following plateau states. The nature of these states, and the associated inverted spectrum radio emission is still unclear, and warrants further study. It is also of interest to clarify whether or not the radio flare which *precedes* the plateau state (Fig. 1) also, as expected, corresponds to a major ejection. Why the accretion disc – jet system in GRS 1915+105 appears to switch so rapidly between major mass ejections, short period (oscillation) instabilities and back again (Fig. 7) is still very uncertain. Atoyán & Aharonian (1997) discuss the disruption of the accretion disc due to recoil momentum from an asymmetric ejection. However, it is difficult to reconcile their model with the apparent very rapid reformation of the (unstable) inner accretion disc after the major (NE+SW) ejection. Finally, it is tempting to ascribe the apparent ‘period’ of the jet bending of ~ 7 days to an orbital period, as was found to be the case for GRO J1655–40, but at present this is no more than speculation.

These MERLIN observations are further evidence that GRS 1915+105 repeatedly produces relativistic ejections of massive clouds of synchrotron-emitting electrons. Our observations of very high proper motions in the inner 0.3 arcsec of the jet show that galactic stellar-mass black holes are capable of accelerating matter to velocities very close to the speed of light.

ACKNOWLEDGEMENTS

We acknowledge the assistance of many people in the triggering and realisation of these observations, including Shane McKie, Richard Ogley and Peter Thomasson. MERLIN is operated as a National Facility by the University of Manchester at the Nuffield Radio Astronomy Laboratories, Jodrell Bank, on behalf of the Particle Physics and Astronomy Research Council (PPARC). We thank the staff at MRAO for maintenance and operation of the Ryle Telescope, which is supported by the PPARC. We also thank the referee for prompt and useful comments. The Green Bank Interferometer is a facility of the National Science Foundation and is currently operated by the National Radio Astronomy Observatory in support of the NASA High Energy Astrophysics programs. Radio astronomy at the Naval Research Laboratory is supported by the Office of Naval Research. We acknowledge the use of quick-look results provided by the ASM/RXTE team. RPF was supported during the period of this research initially by ASTRON grant 781-76-017 and subsequently by EC Marie Curie Fellowship ERBFMBICT 972436. DJM acknowledges support for his research by the European Commission under TMR-LSF contract No. ERBFMGECT950012.

REFERENCES

- Atoyán A.M., Aharonian F.A., 1997, *ApJ*, 490, L149
 Bailyn C.D., Orosz J.A., McClintock J.E., Remillard R.A., 1995, *Nature*, 378, 157
 Bandyopadhyay R., Martini P., Gerard E., Charles P.A., Wagner R.M., Shrader C., Shahbaz T., Mirabel I.F., 1998, *MNRAS*, 295, 623
 Belloni T., Mendez M., King A.R., van der Klis M., van Paradijs J., 1997a, *ApJ*, 479, L145
 Belloni T., Mendez M., King A.R., van der Klis M., van Paradijs J., 1997b, *ApJ*, 488, L109
 Castro-Tirado A., Brandt S., Lund N., 1992, *IAU Circ* 5590
 Cawthorne T.V., Wardle J.F.C., Roberts D.H., Gabuzda D.C., 1993, *ApJ*, 416, 519
 Downes D., Wilson T.L., Bieging J., Wink J., *A&AS*, 1980, 40, 379
 Eikenberry S.S., Matthews K., Morgan E.H., Remillard R.A., Nelson R.W., 1998, *ApJ*, 494, L61
 Feldt M., Stecklum B., Henning Th., Hayward T.L., Lehmann Th., Klein R., 1998, *A&A*, 339, 759
 Fender R.P., Pooley G.G., Brocksopp C., Newell S.J., 1997, *MNRAS*, 290, L65
 Fender R.P., Pooley G.G., 1998, *MNRAS*, 300, 573
 Foster R. S., Waltman E. B., Tavani M., Harmon B. A., Zhang S. N., Paciesas W. S., and Ghigo F. D. 1996, *ApJ*, 467, L81
 Harmon B.A., Deal K.J., Paciesas W.S., Zhang S.N., Robinson C.R., Gerard E., Rodríguez L.F., Mirabel I.F., 1997, *ApJ*, 477, L85
 Harris D.E., Carilli C.L., Perley R.A. 1994, *Nature*, 367, 713
 Hjellming R.M., Rupen M.P., 1995, *Nature*, 375, 464
 Hughes P.A. (editor), 1991, *Beams and Jets in Astrophysics*, CUP
 Kemball A.J., Diamond P.J., Pauliny-Toth I.I.K., 1996, *ApJ*, 464, L55
 Levine A.M., Bradt H., Cui W., Jernigan J.G., Morgan E.H., Remillard R.A., Shirey R., Smith D., 1996, *ApJ*, 469, L33
 Longair M.S., 1994, *High Energy Astrophysics*, Vol 2, 2nd edition, CUP
 Mirabel I.F., Rodríguez L.F., 1994, *Nature*, 371, 46 [MR94]
 Mirabel I.F. et al., 1994, *A&A*, 282, L17

- Mirabel I.F., Rodríguez L.F., Chaty S., Sauvage M., Gerard E., Duc P.-A., Castro-Tirado A., Callanan P., 1996, *ApJ*, 472, L111
- Mirabel I.F., Dhawan V., Chaty S., Rodríguez L.F., Martí J., Robinson C.R., Swank J., Geballe T.R., 1998, *A&A*, 330, L9
- Patnaik A.R., Browne I.W.A., Wilkinson P.N., Wrobel J.M., 1992, *MNRAS* 254, 655
- Pooley G.G., 1995, *I.A.U. Circ* 6269
- Pooley G.G., Fender R.P., 1997, *MNRAS*, 292, 925 [PF97]
- Quirrenbach A., Witzel A., Qian S.J., Krichbaum T., Hummel C.A., Alberdi A., 1989, *A&A* 226, L1
- Rodríguez L.F., Gerard E., Mirabel I.F., Gomez Y., & Velazquez A., 1995, *ApJ Supp.*, 101,173,
- Rodríguez L.F., Mirabel I.F., 1999, *ApJ*, in press [RM99]
- Rupen M.P., Hjellming R.M., Mioduszewski A.J., 1998, *IAU Circ.* 6938
- Sams B., Eckart A., Sunyaev R., 1996, *Nature*, 382, 47
- Tingay S.J. et al., 1995, *Nature*, 374, 141
- Vermeulen R.C., Schilizzi R.T., Spencer R.E., Romney J.D., Fejes J., 1993, *A&A*, 270, 177